

Article

In-Gap Edge and Domain-Wall States in Largely Perturbed Phononic Su–Schrieffer–Heeger Lattices

Amir Rajabpoor Alisepahi¹ and Jihong Ma^{1,2,*} 

¹ Department of Mechanical Engineering, University of Vermont, Burlington, VT 05405, USA; amir.rajabpoor-alisepahi@uvm.edu

² Materials Science Program, University of Vermont, Burlington, VT 05405, USA

* Correspondence: jihong.ma@uvm.edu

Abstract: Topological states of matter have attracted significant attention due to their intrinsic wave-guiding and localization capabilities robust against disorders and defects in electronic, photonic, and phononic systems. Despite the above topological features that phononic crystals share with their electronic and photonic counterparts, finite-frequency topological states in phononic crystals may not always survive. In this work, we discuss the survivability of topological states in Su–Schrieffer–Heeger models with both local and non-local interactions and larger symmetry perturbation. Although such a discussion is still about ideal mass-spring models, the insights from this study set the expectations for continuum phononic crystals, which can further instruct the application of phononic crystals for practical purposes.

Keywords: topological states; phononic crystals; chiral symmetry; phonon bandgap



Citation: Rajabpoor Alisepahi, A.; Ma, J. In-Gap Edge and Domain-Wall States in Largely Perturbed Phononic Su–Schrieffer–Heeger Lattices. *Crystals* **2024**, *14*, 102. <https://doi.org/10.3390/cryst14010102>

Academic Editor: Luis M. Garcia-Raffi

Received: 31 December 2023

Revised: 16 January 2024

Accepted: 20 January 2024

Published: 22 January 2024



Copyright: © 2024 by the authors. Licensee MDPI, Basel, Switzerland. This article is an open access article distributed under the terms and conditions of the Creative Commons Attribution (CC BY) license (<https://creativecommons.org/licenses/by/4.0/>).

1. Introduction

Topological insulators (TIs) are intrinsically electrical insulators with conducting surfaces/edges/corners when interfaced with trivial insulators, including vacuum. These surface/edge/corner states result from TI bulk properties, i.e., topological invariants, and are thus robust against local perturbations and disorders [1], making them ideal candidates for various promising applications in electronics with strict dissipation, especially quantum-computing systems [2]. They have thus attracted significant attention. Moreover, in recent years, these topologically protected non-dissipative localized states have inspired studies of classical analogs of TIs in photonic [3–7], magnetic [8–10], and mechanical [11–17] systems.

In mechanical systems, a similar topological invariant can also be derived from the spectral evolution of eigenvectors of the dynamical matrix (or the compatibility matrix) from a unit cell analysis. The integer topological invariant can then inform the numbers and types of topologically protected surface/edge/corner states confining static deformation [18–22] or vibration [11,13–17,23–25] within a bulk bandgap (which is a frequency range with no eigenfrequency solutions, i.e., bulk wave propagation) when a material/structure with a non-zero topological invariant, i.e., a topologically non-trivial phase, forms a domain wall with another domain characterized by a zero-topological invariant, i.e., a topologically trivial phase, including vacuum. Such a bulk property reflected as surface/edge/corner states at a domain wall or edge is usually referred to as the bulk–edge correspondence.

A commonly used example to illustrate this bulk–edge correspondence is the one-dimensional (1D) Su–Schrieffer–Heeger (SSH) lattice, as shown in Figure 1a. With alternating spring constants connecting identical masses, m , a bulk bandgap can be opened as shown in Figure 1b. It has been well established that the larger the difference in these spring constants, the wider the bandgap we can obtain. In the existing literature, finite-frequency in-gap topological modes are commonly created by seaming two domains with a difference in topology (here, we refer to these as topologically protected domain-wall states (TPDWSs)) [15,17,26], or by simply placing a lattice with a free or fixed edge [27,28],

sometimes cited as “topologically protected edge states” (TPESs) [29–33]. However, as discussed in Refs. [30,31], the existence of these edge states and their frequencies (in case they exist) depend heavily on the boundary conditions in finite lattices, making these edge states less robust. This is because such boundaries perturb the chiral symmetry of the system’s dynamical matrix. Strictly speaking, these edge states are no longer topologically protected due to the loss of chiral symmetry. In fact, this is also the case if a domain boundary is formed between two domains with different topologies when a large perturbation to the unit cell symmetry is introduced. However, this has received much less attention, since most discussions on TPDWSs introduce a small perturbation in spring stiffness to open the bandgap in order to preserve the chiral symmetry to some extent. Nonetheless, a large bandgap is usually desirable in many applications requiring vibration mitigation within a certain frequency range [34–37]. Hence, it is important to identify the conditions for the survivability of the in-gap states. Since these in-gap states are deviations from TPESs or TPDWSs, some topological features at these boundaries still exist even with a large chiral symmetry perturbation.

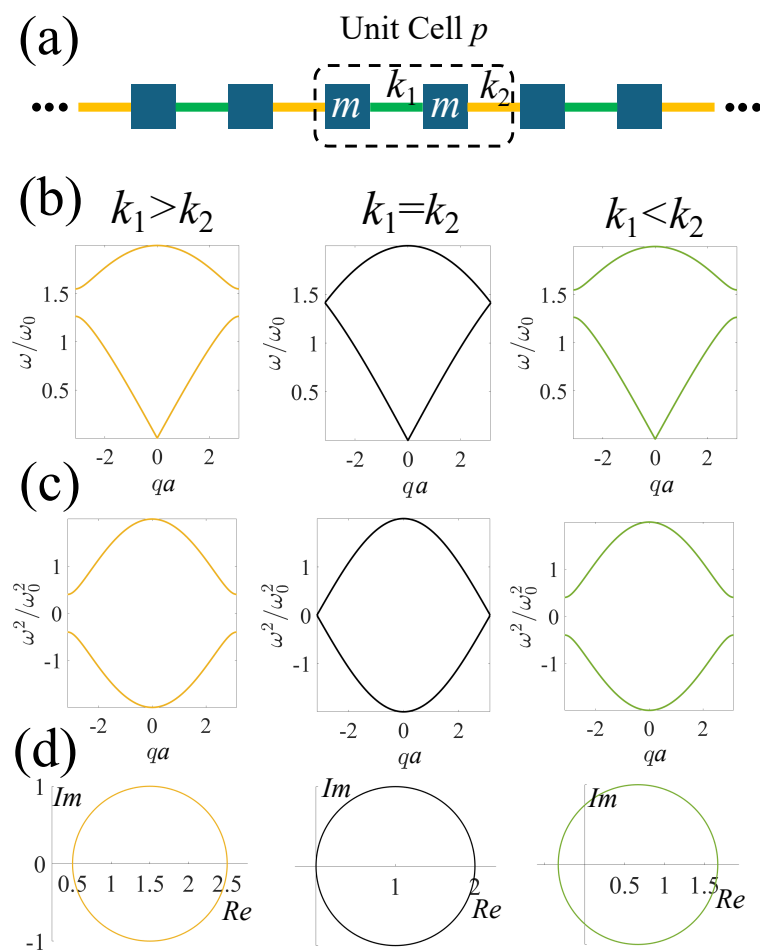


Figure 1. (a) Unit cell (circled in a dashed line) of a chain of identical masses, m , with alternating springs possessing spring constants k_1 (green bars) and k_2 (yellow bars). The unit cell length is a . (b) Phonon dispersion curves. (c) Eigenvalue plots of $\tilde{D}(q)$ denoted as ω^2 (both normalized by $\omega_0 = \sqrt{(k_1 + k_2)/2m}$). (d) Winding paths for $k_1 > k_2$ (e.g., $k_1 = 1.2$ and $k_2 = 0.8$, left); $k_1 = k_2$ (e.g., $k_1 = k_2 = 1$, middle); and $k_1 < k_2$ (e.g., $k_1 = 0.8$ and $k_2 = 1.2$, right) in the unit cell.

In this work, we will delve into SSH systems with large symmetry perturbations at the domain boundary and the unit cell. Simple SSH chains with nearest-neighbor interactions only and more complex SSH networks with beyond-nearest neighbors (BNNs) will both be taken into account, the latter of which has recently gained increasing attention due to their

roton-like dispersion relations similar to those in correlated quantum systems [38–43], as well as their unconventional topological states associated with BNN coupling [17,44–46]. The survivability of the in-gap states will be analyzed, which will further instruct the design of large-bandgap structures in the continuum regime.

2. Results and Discussion

2.1. Su–Schrieffer–Heeger Systems with Nearest-Neighbor Interactions

To simplify the illustration, we only consider displacements of identical masses, m , connected by alternating nearest-neighbor springs with spring constants k_1 and k_2 along the chain, as shown in Figure 1a. The governing equations of a lattice unit cell can be expressed as

$$m\ddot{x}_1^p = k_1(x_2^p - x_1^p) - k_2(x_1^p - x_2^{p-1}), \quad (1)$$

$$m\ddot{x}_2^p = k_2(x_1^{p+1} - x_2^p) - k_1(x_2^p - x_1^p), \quad (2)$$

where displacements of the two masses in the p -th cell are denoted as x_1^p and x_2^p , respectively. The displacements of masses in any unit cell p at time t can be expressed by those within a reference unit cell using a plane-wave solution in combination with Bloch–Floquet periodic boundary conditions:

$$\mathbf{x}^p(t) = \tilde{\mathbf{x}}(q)e^{i(pqa - \omega t)}, \quad (3)$$

where ω is the vibration frequency; \mathbf{x}^p is the displacements of the p -th cell with $\mathbf{x}^p = [x_1^p, x_2^p]$; q is the wave number, which is inversely proportional to the wavelength λ , i.e., $q = 2\pi/\lambda$; a denotes the lattice constant; and $\tilde{\mathbf{x}}(q)$ is displacements within the reference unit cell. Substituting this expression into Equations (1) and (2) gives

$$[D(q) - \omega^2 m]\tilde{\mathbf{x}}(q) = 0, \quad (4)$$

where $D(q)$ is the stiffness (or dynamical) matrix of the periodic system

$$D(q) = \begin{bmatrix} k_1 + k_2 & -k_1 - k_2 e^{-iqa} \\ -k_1 - k_2 e^{iqa} & k_1 + k_2 \end{bmatrix}. \quad (5)$$

The square root of the eigenvalues of $D(q)$ gives the phonon band diagram, as presented in Figure 1b. With $k_1 = k_2$, there is no bandgap between the two bands. When $k_1 \neq k_2$, a bandgap is created between the two phonon bands due to the breaking of the unit cell space-inversion symmetry (SIS). Although the bandgap does not change if $k_1 > k_2$ or vice versa, the two choices of gauge result in two different topological states since the transition from one to another unavoidably passes the non-gap state, i.e., non-gapped transition, as shown in the middle panels of Figure 1b–d. To characterize the topology of such a 1D system, the Zak phase [47] measuring the rotation of eigenvectors in the unit cell, or the winding number n are often evaluated, as shown in Figure 1d. The latter of these is defined as

$$n = \int_{-\pi/a}^{\pi/a} \frac{1}{4\pi i} \text{tr}[\sigma_z \tilde{D} \partial_q \tilde{D}] dq, \quad (6)$$

where σ_z is the unitary matrix, and \tilde{D} is the chiral matrix $D(q)$ after subtracting all diagonal elements:

$$\tilde{D}(q) = D(q) - (k_1 + k_2)\mathbf{I}, \quad (7)$$

where \mathbf{I} is the identity matrix. The eigenvalues of $\tilde{D}(q)$ appear to be symmetric about the x -axis, as shown in Figure 1c.

As we can see, when $k_1 > k_2$, $n = 0$, indicating a trivial intra-cell-hopping phase. On the contrary, when $k_1 < k_2$, $n = 1$, suggesting a topologically non-trivial inter-cell-hopping phase. Such a difference in topology due to gauge choice suggests that when connecting

two domains with these two different topologies, there exists a localized mode with a frequency located within the bandgap at the domain wall.

In this section, we will discuss the effect of the boundary conditions on the existence of in-gap states when the simple mass-spring lattice shown in Figure 1a is interfaced with a vacuum (Section 2.1.1, In-Gap Edge States in Finite Lattices) and with a domain possessing an opposite gauge in the unit cell (Section 2.1.2, In-Gap Domain-Wall States in Infinite Lattices) with various δk values characterizing the difference between k_1 and k_2 , defined as $k_1 = 1 - \delta k$ and $k_2 = 1 + \delta k$. Here, we consider a wide range of δk values, up to ± 0.9 , which is 90% of the average spring stiffness (we set $\frac{k_1+k_2}{2} = 1$). Such a big difference in the spring constants will create a large bulk bandgap, which, as mentioned in the Introduction, is desirable for many applications. However, the survivability of the in-gap states depends on the specific boundary condition.

2.1.1. In-Gap Edge States in Finite Lattices

Although the number of unit cells should be approximate to infinity in the finite lattice or supercell to allow for sufficient spatial decay from the edge/domain wall for an in-gap state, in our previous study of the effect of third-nearest neighbors (TNNs) on TPDWSs, we were able to identify TPDWSs with only eight unit cells in each domain in our 3D model and experiments [17]. Since, in this work, we are interested in observing finite lattices or supercells with domain walls not too far apart, we take the finite lattice containing 20 unit cells presented in Figure 1a with free boundaries, as shown in Figure 2a. The stiffness matrix of such a finite system is

$$D(q) = \begin{bmatrix} k_1 & -k_1 & 0 & \dots & 0 & 0 & 0 \\ -k_1 & k_1 + k_2 & -k_2 & \dots & 0 & 0 & 0 \\ 0 & -k_2 & k_1 + k_2 & \dots & 0 & 0 & 0 \\ \vdots & \vdots & \vdots & \ddots & \vdots & \vdots & \vdots \\ 0 & 0 & 0 & \dots & k_1 + k_2 & -k_2 & 0 \\ 0 & 0 & 0 & \dots & -k_2 & k_1 + k_2 & -k_1 \\ -0 & 0 & 0 & \dots & 0 & -k_1 & k_1 \end{bmatrix}. \quad (8)$$

As we can see, $D(q)$ is not a chiral matrix due to the non-identical diagonal elements at the two free boundaries. Hence, no in-gap states exist, as shown in Figure 2a–d, regardless of δk .

The in-gap edge states can be easily acquired by fixing the two ending masses with a spring, $k_{fix} = k_2$, connected to a wall, as shown in Figure 2e, making the $D(q)$ chiral:

$$D(q) = \begin{bmatrix} k_1 + k_2 & -k_1 & 0 & \dots & 0 & 0 & 0 \\ -k_1 & k_1 + k_2 & -k_2 & \dots & 0 & 0 & 0 \\ 0 & -k_2 & k_1 + k_2 & \dots & 0 & 0 & 0 \\ \vdots & \vdots & \vdots & \ddots & \vdots & \vdots & \vdots \\ 0 & 0 & 0 & \dots & k_1 + k_2 & -k_2 & 0 \\ 0 & 0 & 0 & \dots & -k_2 & k_1 + k_2 & -k_1 \\ -0 & 0 & 0 & \dots & 0 & -k_1 & k_1 + k_2 \end{bmatrix}. \quad (9)$$

Subtracting the diagonal elements as in Equation (7) also gives us a chiral matrix $\tilde{D}(q)$. In this case, as long as the SSH terminating cells present a non-trivial gauge, i.e., $k_1 < k_2$ or $\delta k > 0$, and are interfaced with a vacuum—a trivial domain—the in-gap edge states are guaranteed to exist regardless of the magnitude of δk , as evident in Figure 2f–h. Moreover, due to the strict chiral symmetry Equation (9) presents, all the in-gap edge states are located exactly at $\omega/\omega_0 = \sqrt{(k_1 + k_2)/m}$ in the eigenfrequency plot in Figure 2f, or $\omega^2/\omega_0^2 = 0$ in the $\tilde{D}(q)$ eigenvalue plot in Figure 2g, which we refer to as the mid-gap state in our discussion. These in-gap edge states completely follow the definition of TPESs, also known as the Jackiw–Rebbi zero modes [48].

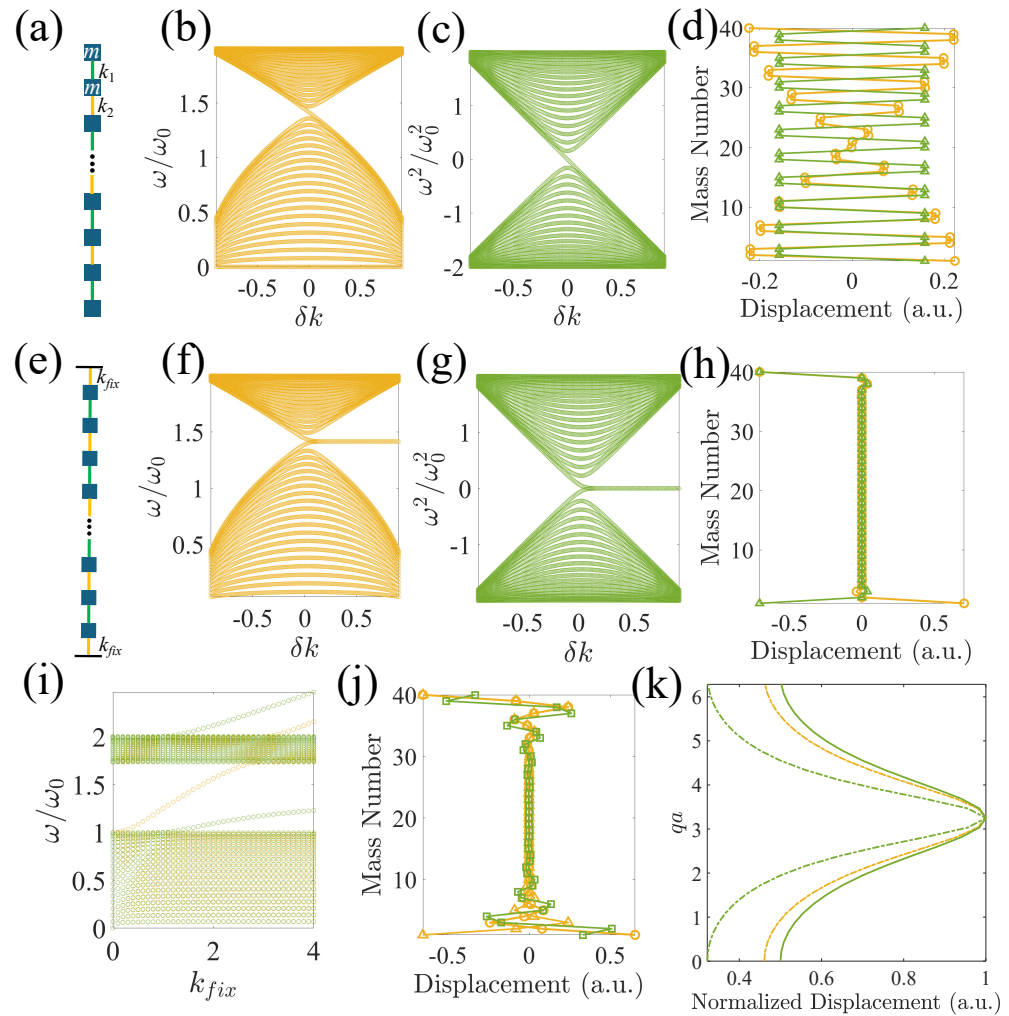


Figure 2. (a) A finite lattice containing 20 unit cells of identical masses, m , with alternating springs possessing spring constants k_1 (green bars) and k_2 (yellow bars). $k_1 = 1 - \delta k$ and $k_2 = 1 + \delta k$. (b) Normalized eigenfrequencies of the finite lattice in (a). (c) Normalized eigenvalues of the stiffness matrix of (a) after subtracting $2 \cdot \mathbf{I}$, i.e., $\tilde{D}(q) = D(q) - (k_1 + k_2) \cdot \mathbf{I}$, to better evaluate the deviation of the in-gap states from the midgap if they exist. (d) Twentieth (yellow circles) and twenty-first (green triangles) eigenmodes when $\delta k = 0.9$. (e) Connecting the two ends of the finite lattice to a wall by springs with a constant $k_{fix} = k_2$. (f) Normalized eigenfrequencies of the finite lattice in (e). (g) Normalized eigenvalues of the stiffness matrix of (e) after subtracting $2 \cdot \mathbf{I}$. (h) Twentieth (yellow circles) and twenty-first (green triangles) eigenmodes when $\delta k = 0.9$. (i) Normalized eigenfrequencies of the stiffness matrix of (e) with varying k_{fix} and fixed k_1 and k_2 (yellow— $\delta k = 0.5$, green— $\delta k = -0.5$). (j) In-gap eigenmodes of $\delta k = 0.5$ (yellow circles and triangles) and $\delta k = -0.5$ (green squares) when $k_{fix} = 2$. (k) Spatial Fourier transform of mode shapes of the lattice with $\delta k = 0.5$ and $k_{fix} = k_2$ (solid green), $\delta k = 0.5$ and $k_{fix} = 2$ (dashed yellow), and $\delta k = -0.5$ and $k_{fix} = 2$ (dashed green).

However, despite being topologically protected, these TPESs are prone to boundary conditions. A small perturbation at the edges will make the TPESs drift away from the mid-gap state, or even disappear, as shown in Figure 2i. Thus, topology alone can no longer guarantee the existence of TPESs. The chiral symmetry of the entire system is crucial to achieve TPESs. On the other hand, even when the chain terminates with topologically trivial unit cells on both ends, one in-gap state on both ends may still emerge with a sufficiently large k_{fix} , as presented in Figure 2i. This in-gap state, nonetheless, is merely a trivial edge state due to the termination of periodicity. As can be seen from the spatial Fourier transform (SFT) of these edge states, when it is a strict TPES, the SFT of the mode

shape when $\delta k = 0.5$ and $k_{fix} = k_2$ presents the widest peak at $qa = \pi$. With the same δk , which ensures the same topology, despite significantly increasing k_{fix} to 2, which deviates the edge state from the mid-gap frequency, its SFT is only slightly narrower than that of the strict TPES. In contrast, when making the lattice topology trivial by reversing δk to -0.5 , although an in-gap state emerges with a large k_{fix} , the SFT is significantly (approximately 60%) narrower than that of the TPES, indicating a much slower spatial decay (or a stronger leakage into the bulk) than the TPES. Here, we use the mid-peak widths of the SFT to calibrate the spatial decay speed. The wider these peaks are, the faster the spatial decay of the edge/domain-wall modes into the bulk, and vice versa. Hence, the topological-like in-gap state, even with a large perturbation, is more robust in localizing edge states than the trivial in-gap state.

2.1.2. In-Gap Domain-Wall States in Infinite Lattices

When seaming two topologically different domains, as shown in Figure 3a, to obtain TPDWs, the chiral symmetry of the dynamical matrix, $D(q)$, of the entire system must also be maintained. Without any modification, the $D(q)$ of the supercell shown in Figure 3a, in which the Bloch–Floquet boundary conditions are applied to the top and bottom masses, is written as

$$D(q) = \begin{bmatrix} k_1 + k_2 & -k_1 & 0 & & & & 0 & 0 & -k_2 e^{-iqa} \\ -k_1 & k_1 + k_2 & -k_2 & & & & 0 & 0 & 0 \\ 0 & -k_2 & k_1 + k_2 & & & & 0 & 0 & 0 \\ & & & \ddots & & & & & \\ & \vdots & & -k_1 & 2k_1 & -k_1 & & \vdots & \\ & & & & & \ddots & & & \\ 0 & 0 & 0 & & & & k_1 + k_2 & -k_2 & 0 \\ 0 & 0 & 0 & & & & -k_2 & k_1 + k_2 & -k_1 \\ -k_2 e^{iqa} & 0 & 0 & & & & 0 & -k_1 & k_1 + k_2 \end{bmatrix}, \quad (10)$$

which is not a chiral matrix due to the domain-wall mass connected to k_1 on both sides. Although we can achieve a chiral matrix by pinning the domain-wall mass, it is not realistic in practice and highly challenging when $k_1 > k_2$.

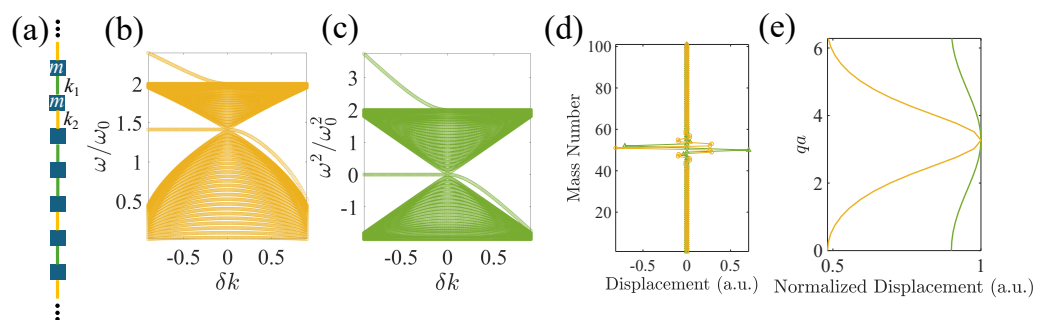


Figure 3. (a) An infinite lattice with a supercell containing 101 identical masses, m , with alternating springs possessing spring constants k_1 (green bars) and k_2 (yellow bars) forming an interface at the central mass, about which is connected k_1 on both sides. $k_1 = 1 - \delta k$ and $k_2 = 1 + \delta k$. (b) Normalized eigenfrequencies of the finite lattice in (a). (c) Normalized eigenvalues of the stiffness matrix of (a) after subtracting $2 \cdot I$. (d) Supercell eigenmodes when $\delta k = -0.9$ (green triangles) and $\delta k = 0.9$ (yellow circles). (e) Spatial Fourier transform of the mode shapes in (d).

When the difference between k_1 and k_2 , or $|\delta k|$, is small, $D(q)$ does not significantly deviate from a chiral matrix; thus, the in-gap state is still adjacent to the middle of the bandgap, as shown in Figure 3b,c. However, when k_1 and k_2 are largely different, $D(q)$ can no longer be approximated as a chiral matrix. Interestingly, when $\delta k < 0$, i.e., $k_1 > k_2$, the

in-gap state is intact. The breaking of the chiral symmetry of $D(q)$ results in an additional trivial edge mode arising above the upper limit of the bulk mode. On the contrary, when $\delta k > 0$, the in-gap state drops quickly near the lower bulk mode as δk increases. Although unlike in finite lattices, such an in-gap state always survives, it is not easy to detect due to its proximity to the bulk mode. Mode shapes when $\delta k = \pm 0.9$ are presented in Figure 3d. The mid-gap state when $\delta k = -0.9$ decays rapidly due to a large bandgap. In contrast, when $\delta k = 0.9$, the domain-wall state decays slowly into the bulk since its frequency is merely slightly above the bulk mode. A quantitative comparison of the spatial decay speed can be obtained from the SFT of these mode shapes from the domain-wall mass into the bulk presented in Figure 3e, which shows a much wider peak when $\delta k = -0.9$ since the domain-wall state resides in the middle of a large bandgap due to severe perturbation in k , while a narrower peak is shown when $\delta k = 0.9$, indicating a slower spatial decay into the bulk since the in-gap state is close to the lower bulk bands.

2.2. Su–Schrieffer–Heeger Systems with Beyond-Nearest-Neighbor Interactions

Introducing non-local or BNN interactions further complicates the discussion. In this section, we will discuss systems with identical TNNs where the nearest neighbors are non-identical, i.e., $k'_1 = k'_2$ and $k_1 \neq k_2$, and vice versa, as shown in Figure 4.

The additional TNNs connect the current cell, p , with the one beyond its immediate neighbors, i.e., $p \pm 2$, modifying the governing equations as follows:

$$m\ddot{x}_1^p = k_1(x_2^p - x_1^p) - k_2(x_1^p - x_2^{p-1}) + k'_1(x_2^{p+1} - x_1^p) - k'_2(x_1^p - x_2^{p-2}), \quad (11)$$

$$m\ddot{x}_2^p = k_2(x_1^{p+1} - x_2^p) - k_1(x_2^p - x_1^p) + k'_2(x_1^{p+2} - x_2^p) - k'_1(x_2^p - x_1^{p-1}). \quad (12)$$

Plugging in Equation (3), we obtain the following stiffness matrix:

$$D(q) = \begin{bmatrix} k_1 + k_2 + k'_1 + k'_2 & -k_1 - k_2 e^{-iqa} - k'_1 e^{iqa} - k'_2 e^{-2iqa} \\ -k_1 - k_2 e^{iqa} - k'_1 e^{-iqa} - k'_2 e^{2iqa} & k_1 + k_2 + k'_1 + k'_2 \end{bmatrix}. \quad (13)$$

The chiral matrix $\tilde{D}(q)$ can then be obtained from

$$\tilde{D}(q) = D(q) - (k_1 + k_2 + k'_1 + k'_2)\mathbf{I}. \quad (14)$$

The additional exponential terms in Equations (11) and (12), or the off-diagonal terms in $D(q)$ Equation (13) due to TNNs yield the bending of the dispersion curves in the irreducible Brillouin zone (IBZ), as shown in Figure 4b,c, also known as roton-like acoustic dispersions, similar to those discovered at cryogenic temperatures in correlated quantum systems [38–43].

Although phonon dispersions due to different nearest neighbors and TNNs are almost identical, their winding paths differ significantly. When $k_1 > k_2$ and $k'_1 = k'_2$, $n = 0$ with two extra local loops formed along the path, while when $k_1 = k_2$ and $k'_1 > k'_2$, $n = -1$ since the circuit winds about the origin in the opposite direction (clockwise) to that of the main path. Such a difference in winding number indicates that the former lattice is topologically trivial, while the latter is non-trivial. On the contrary, when $k_1 < k_2$ and $k'_1 = k'_2$, $n = 1$ with three local loops formed along the path, while when $k_1 = k_2$ and $k'_1 < k'_2$, the circuit winds about the origin twice counterclockwise; thus, $n = 2$, indicating that both are non-trivial. This suggests that when interfacing the lattice of $n \neq 0$ with a vacuum or a topologically trivial domain, n edge/domain-wall states should exist. However, previously, we demonstrated that this is not necessarily correct. We mathematically demonstrated that the number of domain-wall states when seaming two topologically different domains is determined by the number of band crossings when $k_1 = k_2$ and $k'_1 = k'_2$ within the IBZ, or Dirac points, which is the phonon realization of the Jackiw–Rebbi theory [48]. We found that the actual number of TPDWSs can be characterized by the Berry connection calculated from the integrand of Equation (6), or local winding numbers, instead of the total winding numbers over the IBZ [17]. Nonetheless, the total winding numbers across the whole IBZ as

shown in Figure 4d may still inform the number of edge states when a lattice is terminated and interfaced with a vacuum.

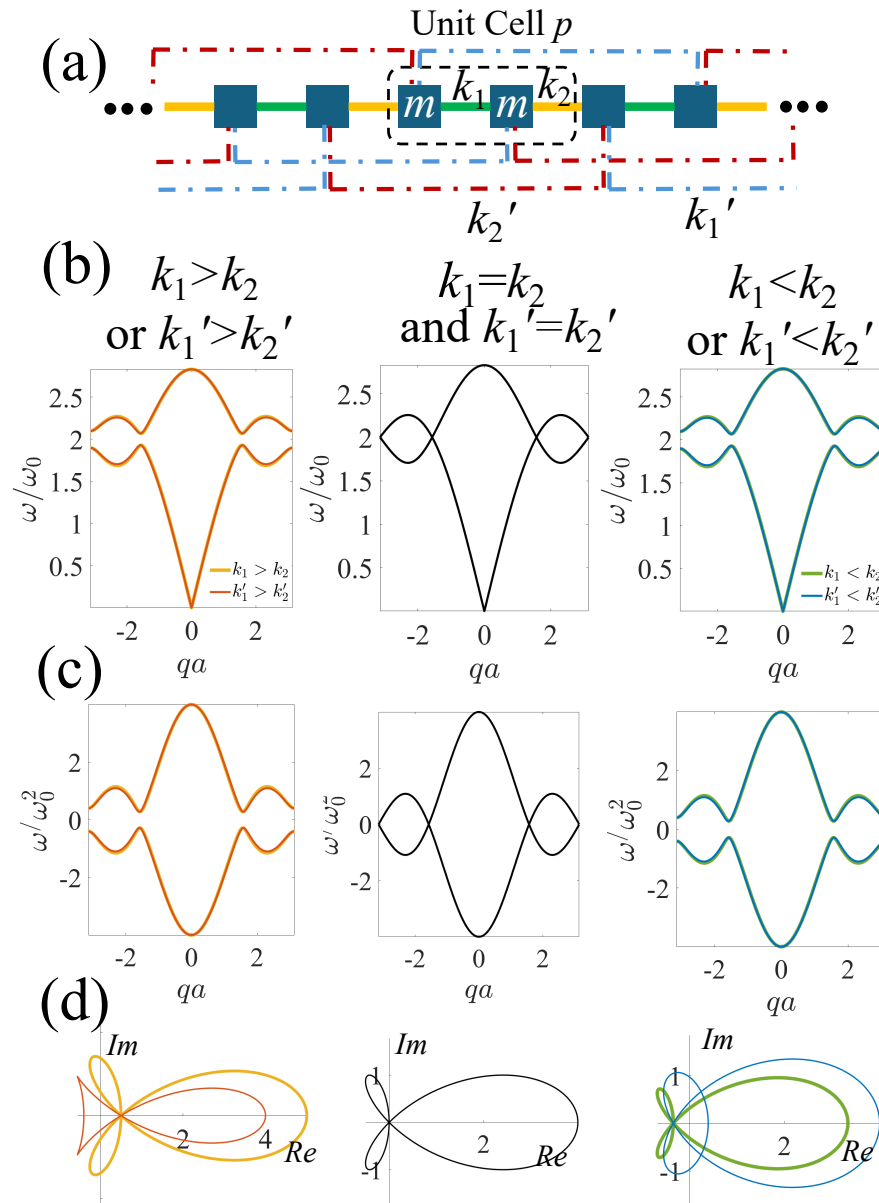


Figure 4. (a) Unit cell (circled in a dashed line) of a chain of identical masses, m , with alternating springs possessing spring constants k_1 (green bars) and k_2 (yellow bars) connecting the nearest neighbors, and k_1' (blue dashed lines) and k_2' (red dashed lines) connecting the third-nearest neighbors. The unit cell length is a . (b) Phonon dispersion curves. (c) Eigenvalue plots of $\tilde{D}(q)$ denoted as ω^2 (both normalized by $\omega_0 = \sqrt{(k_1 + k_2)/2m}$). (d) Winding paths for $k_1 > k_2$ (e.g., $k_1 = 1.2$ and $k_2 = 0.8$) and $k_1' = k_2' = 1$ (yellow curves in the left panel); $k_1 = k_2 = 1$ and $k_1' > k_2'$ (e.g., $k_1' = 1.2$ and $k_2' = 0.8$) (red curves in the left panel); $k_1 = k_2 = k_1' = k_2' = 1$ (black curves in the middle panel); $k_1 < k_2$ and $k_1' = k_2'$ (green curves in the right panel); and $k_1 = k_2$ and $k_1' < k_2'$ (blue curves in the right panel).

In this section, we will discuss the effect of a combination of the spring difference (both δk and $\delta k'$, the latter of which is defined as $k_1' = 1 + \delta k'$ and $k_2' = 1 - \delta k'$) and the boundary conditions on the existence of in-gap states when the mass-spring lattice with TNNs shown in Figure 4a is interfaced with a vacuum (Section 2.2.1) and with a topologically different domain (Section 2.2.2). We consider the scenarios across a wide range of both δk and $\delta k'$,

up to 0.9, which opens up a large bandgap. The conditions of maintaining the in-gap states will be explored.

2.2.1. In-Gap Edge States in Finite Lattices with Third-Nearest Neighbors

Taking a finite lattice containing 20 unit cells with free boundaries, as shown in Figure 5a, yields the following stiffness matrix:

$$D(q) = \begin{bmatrix} k_1 + k'_1 & -k_1 & 0 & 0 & 0 & 0 \\ -k_1 & k_1 + k_2 + k'_2 & -k_2 & \dots & 0 & 0 \\ 0 & -k_2 & k_1 + k_2 + k'_1 & 0 & 0 & 0 \\ \vdots & \vdots & \vdots & \ddots & \vdots & \vdots \\ 0 & 0 & 0 & k_1 + k_2 + k'_1 & -k_2 & 0 \\ 0 & 0 & 0 & \dots & -k_2 & k_1 + k_2 + k'_2 & -k_1 \\ -0 & 0 & 0 & 0 & 0 & -k_1 & k_1 + k'_1 \end{bmatrix}. \quad (15)$$

Again, $D(q)$ is not a chiral matrix due to non-identical diagonal elements close to the two free boundaries. Therefore, we expect there to be no in-gap states. However, this is not the case when $k_1 \neq k_2$ and $k'_1 = k'_2 = 1$, as shown in Figure 5b–d. On the other hand, when $k_1 = k_2 = 1$ and $k'_1 \neq k'_2$, there are no in-gap states (Figure 6a–d), consistent with the observation when masses are only connected by nearest neighbors, as in Figure 2a–d. In the former scenario, although these in-gap states are indeed edge states, the two in-gap mode numbers are 22 and 23 when $\delta k > 0$, and 21 and 22 when $\delta k < 0$. In the case of topological in-gap states, the mode numbers should be 20 and 21 for a finite chain containing 20 unit cells. In addition, there is more leakage of the edge modes into the bulk compared to those shown in Figure 5h when the edges are fixed so that $D(q)$ and $\tilde{D}(q)$ (as defined in Equation (14)) are chiral:

$$\tilde{D}(q) = \begin{bmatrix} 0 & -k_1 & 0 & -k'_1 & 0 & 0 & 0 & 0 \\ -k_1 & 0 & -k_2 & 0 & \dots & 0 & 0 & 0 \\ 0 & -k_2 & 0 & -k_1 & 0 & 0 & 0 & 0 \\ \vdots & \vdots & \vdots & \vdots & \ddots & \vdots & \vdots & \vdots \\ 0 & 0 & 0 & 0 & -k_1 & 0 & -k_2 & 0 \\ 0 & 0 & 0 & 0 & \dots & 0 & -k_2 & 0 \\ 0 & 0 & 0 & 0 & -k'_1 & 0 & -k_1 & 0 \end{bmatrix}, \quad (16)$$

as shown in Figure 5e. Hence, the two in-gap edge states in the lattice with free boundaries shown in Figure 5a–d are trivial edge modes, whose existence is independent of its topology.

On the other hand, when fixing the masses near the two edges with appropriate springs to the ground/wall to make $\tilde{D}(q)$ chiral as in Equation (16), the number of TPESs appear exactly as predicted by their corresponding winding numbers. When $k_1 > k_2$ and $k'_1 = k'_2$, there are no in-gap states since $n = 0$, while when $k_1 < k_2$ and $k'_1 = k'_2$, one in-gap state exists at each edge, matching $n = 1$, as shown in Figure 5f,g, and they are thus TPESs. The SFT of these edge states from the edge to the bulk shown in Figure 5i reveals that the edge modes shown in Figure 5d present over 30% more leakage into the bulk than the TPES in Figure 5h according to the mid-peak widths of the SFT, further demonstrating the vibration localization capabilities of TPESs compared to trivial edge states. Similarly, when $k'_1 > k'_2$ and $k_1 = k_2$, $n = -1$, corresponding to the two mid-gap states when $\delta k' < 0$ (Figure 6g). The opposite arrangement of TNNs, i.e., $\delta k' > 0$ yields two edge states at each end, as shown in Figure 6h, matching its topological invariant, $n = 2$. The SFTs of all the TPESs visualized in Figure 6g,h are shown in Figure 6i, presenting much wider peaks than their counterparts in lattices with free ends shown in Figure 6c,d, indicating that all these TPESs are indeed localized on the edges even with a large $\delta k'$. It is also worth noting that the SFTs of both edge and bulk modes with TNNs show major peaks at $qa = 2\pi/3$ and $5\pi/3$, instead of at $qa = \pi$, as demonstrated in Figure 2k. This is because when introducing

TNNs with $k' > 1/3k$, extra Dirac points emerge within the IBZ. With $\delta k \neq 0$ or $\delta k' \neq 0$, the bandgap at these additional Dirac points opens more slowly than those at $qa = \pi$. Thus, the phonon bands close to this bandgap are more associated with these Dirac points, resulting in SFT peak positions matching their wavenumbers.

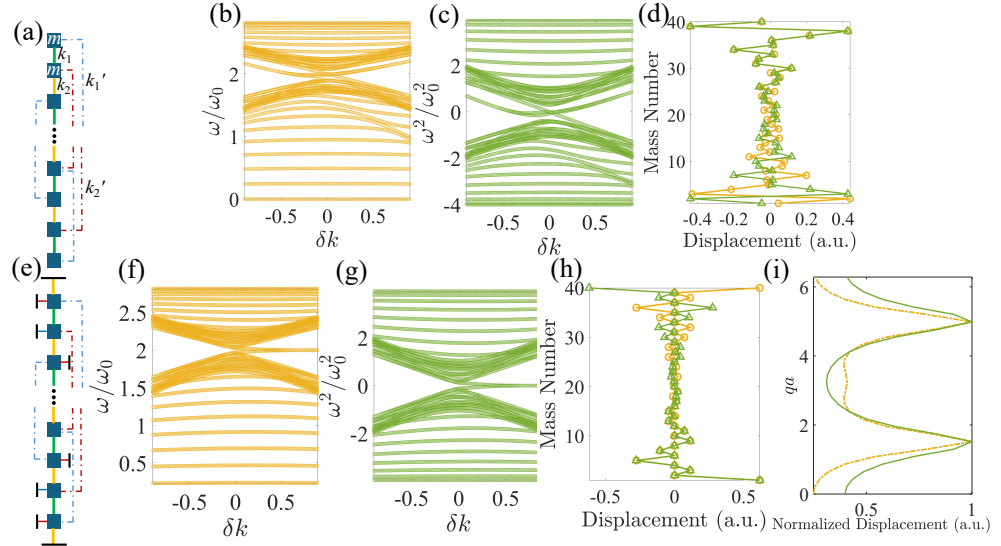


Figure 5. (a) A finite lattice containing 20 unit cells of identical masses, m , with alternating springs possessing spring constants k_1 (green bars) and k_2 (yellow bars) connecting the nearest neighbors, and k'_1 (blue dashed lines) and k'_2 (red dashed lines) connecting the third-nearest neighbors. δk is defined as $k_1 = 1 - \delta k$ and $k_2 = 1 + \delta k$. Here, we consider $k'_1 = k'_2$. (b) Normalized eigenfrequencies of the finite lattice in (a). (c) Normalized eigenvalues of the stiffness matrix of (a) after subtracting $4 \cdot \mathbf{I}$. (d) Twenty-second (yellow circles) and twenty-third (green triangles) eigenmodes when $\delta k = 0.9$. (e) Connecting the two ends of the finite lattice to a wall by springs with spring constants $k_2 + k'_2$, k'_1 , and k'_2 to the first, second, and third masses from the edges, respectively. (f) Normalized eigenfrequencies of the finite lattice in (e). (g) Normalized eigenvalues of the stiffness matrix of (e) after subtracting $4 \cdot \mathbf{I}$. (h) Twentieth (yellow circles) and twenty-first (green triangles) eigenmodes when $\delta k = 0.9$. (i) Spatial Fourier transform of the mode shapes shown in (d) (yellow dashed) and (h) (green solid) from the edge to the bulk.

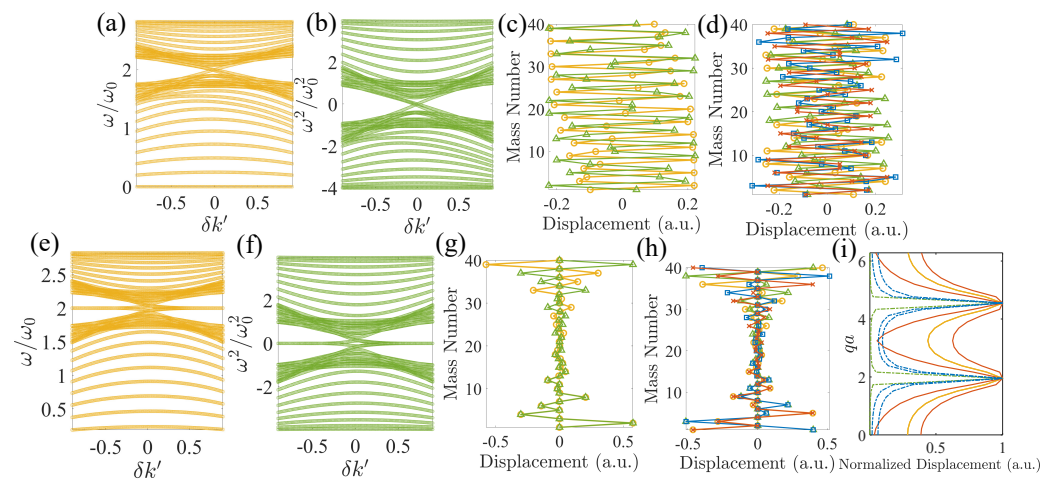


Figure 6. (a) Normalized eigenfrequencies of the finite lattice in Figure 5a with $k_1 = k_2$, $k'_1 = 1 - \delta k'$, and $k'_2 = 1 + \delta k'$. (b) Normalized eigenvalues of the stiffness matrix from the same setup as in (a) after subtracting $4 \cdot \mathbf{I}$. (c,d) Twentieth to twenty-third mode shapes (yellow circles, green triangles, blue squares, and red crosses, respectively) when (c) $\delta k' = -0.9$ (only twentieth and twenty-first modes are shown) and (d) $\delta k' = 0.9$. (e) Normalized eigenfrequencies of the finite lattice in Figure 5e with $k_1 = k_2$, $k'_1 = 1 - \delta k$, and $k'_2 = 1 + \delta k$. (f) Normalized eigenvalues of the stiffness matrix from

the same setup as (e) after subtracting $4 \cdot \mathbf{I}$. (g,h) Twentieth to twenty-third mode shapes (yellow circles, green triangles, blue squares, and red crosses, respectively) when (c) $\delta k' = -0.9$ (only twentieth and twenty-first modes are shown) and (d) $\delta k' = 0.9$. (i) Spatial Fourier transform of the mode shapes shown in (c) (green dashed), (d) (blue dashed), (g) (yellow solid), and (h) (red solid) from the edge to the bulk.

2.2.2. In-Gap Domain-Wall States in Infinite Lattices with Third-Nearest Neighbors

By seaming two domains of lattices with different winding numbers, we can, again, form a domain wall, as shown in Figure 7a. Nonetheless, with the incorporation of TNNs, the domain wall is not a single mass as shown in Figure 3a. Here, the interfacial mass connected by k_1 on both sides serves as the domain-wall mass for the nearest neighbors. This domain-wall mass is also connected by k'_1 on both sides. One additional mass on each side of this domain-wall mass is connected by k'_2 on both sides. Hence, these three masses, altogether, serve as the domain-wall mass for the TNNs. $\tilde{D}(q)$ is then written as

$$\tilde{D}(q) = \begin{bmatrix} 0 & -k_1 & 0 & & & -k'_2 e^{-iqa} & 0 & -k_2 e^{-iqa} \\ -k_1 & 0 & -k_2 & \dots & & 0 & -k'_1 e^{-iqa} & 0 \\ 0 & -k_2 & 0 & & & 0 & 0 & -k'_2 e^{-iqa} \\ & & & \ddots & & & & \\ & & & k'_2 - k'_1 & -k_1 & 0 & & \\ & \vdots & & -k_1 & k_1 - k_2 + k'_1 - k'_2 & -k_1 & \vdots & \\ & & & 0 & -k_1 & k'_2 - k'_1 & & \\ & & & & & \ddots & & \\ -k'_2 e^{iqa} & 0 & 0 & & & 0 & -k_2 & 0 \\ 0 & -k'_1 e^{iqa} & 0 & \dots & & -k_2 & 0 & -k_1 \\ -k_2 e^{iqa} & 0 & -k'_2 e^{iqa} & & & 0 & -k_1 & 0 \end{bmatrix}. \quad (17)$$

As we can see, the spring arrangements at the three domain-wall masses prevent $\tilde{D}(q)$ from being chiral. Unless they are connected by extra springs to a fixed wall to remove the three non-zero diagonal elements in Equation (17), which is not practical, especially when $k'_2 > k'_1$ or $k_1 + k'_1 > k_2 + k'_2$, we expect to observe the strong deviation of the in-gap states from the mid-gap.

In the case of $k'_1 = k'_2 = 1$, we previously demonstrated that the winding numbers shown in Figure 4d can no longer correctly predict the number of TPDWSs. Instead, local winding numbers derived from the Berry connection inform us of three TPDWSs if $\tilde{D}(q)$ is set to be chiral [17]. Without any modification around the domain wall, as δk increases, although the three in-gap states still exist, as shown in Figure 7b,c, when $\delta k < 0$, only one in-gap state remains at the mid-gap, and two of them become extremely close to the bulk modes, resulting in more leakage of the domain-wall states into the bulk, as shown in Figure 7d. When $\delta k > 0$, all three in-gap states survive in the bandgap, but with a large deviation from the mid-gap. Thus, the domain-wall states still leak into the bulk, as shown in Figure 7e, compared to those with a small δk . The SFT of these in-gap states in Figure 7f shows that, indeed, the mid-gap mode when $\delta k = -0.9$ has two wider peaks at $qa = 2\pi/3$ and $5\pi/3$, indicating faster spatial decay than other in-gap states. Note that despite the large deviation from the mid-gap frequency, all three domain-wall states remain within the bandgap, matching the local winding number prediction we proposed in our previous work [17].

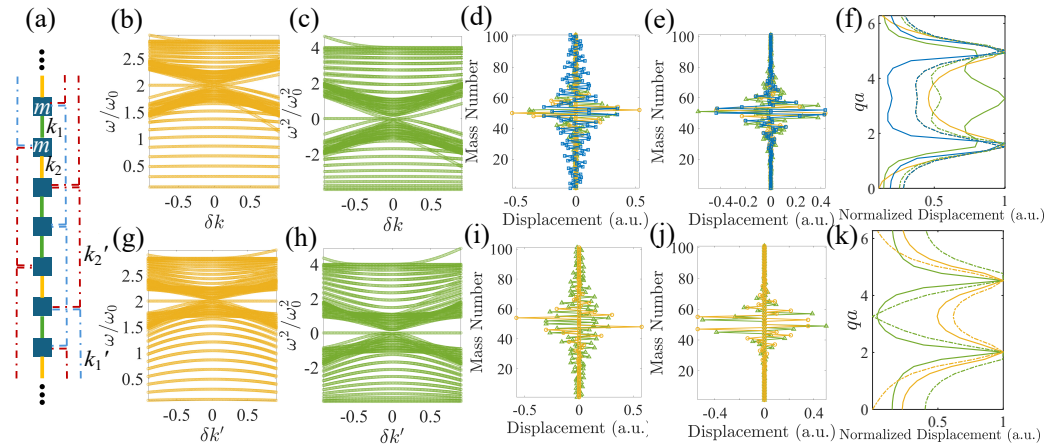


Figure 7. (a) An infinite lattice with a supercell containing 101 identical masses, m , with alternating nearest-neighbor springs possessing spring constants k_1 (green bars) and k_2 (yellow bars) ($k_1 = 1 - \delta k$ and $k_2 = 1 + \delta k$), and third-nearest-neighbor springs k'_1 (blue dashed lines) and k'_2 (red dashed lines) ($k'_1 = 1 - \delta k'$ and $k'_2 = 1 + \delta k'$). A domain wall is formed at the central mass, about which is connected $k_1 + k'_1$ on both sides. The two masses about the domain wall are connected by $k_1 + k_2 + 2 * k'_2$. (b) Normalized eigenfrequencies of the finite lattice in (a) when $k'_1 = k'_2$. (c) Normalized eigenvalues of the stiffness matrix of (a) when $k'_1 = k'_2$ after subtracting $4 \cdot \mathbf{I}$. (d,e) Fiftieth to fifty-second modes shown as green triangles, yellow circles, and blue squares, respectively, when (d) $\delta k = -0.9$ and (e) $\delta k = 0.9$. (f) Spatial Fourier transform of the in-gap 50th (yellow), 51st (green), and 52nd (blue) modes in (d) (solid) and (e) (dashed). Note that the yellow dashed curve overlaps with the blue dashed curve. (g) Normalized eigenfrequencies of the finite lattice in (a) when $k_1 = k_2$. (h) Normalized eigenvalues of the stiffness matrix of (a) when $k_1 = k_2$ after subtracting $4 \cdot \mathbf{I}$. (i,j) Fifty-first and fifty-second modes shown as green triangles and yellow circles, respectively, when (i) $\delta k = -0.9$ and (j) $\delta k = 0.9$. (k) Spatial Fourier transform of the in-gap 51st (green) and 52nd (yellow) modes shown in (i) (solid) and (j) (dashed).

As we vary $\delta k'$ while keeping $k_1 = k_2 = 1$, both the winding number and Berry connection calculation predict that there should be three in-gap states at the domain wall. However, according to Figure 7g,h, this is only the case when $\delta k' \rightarrow 0$. As $|\delta k'|$ increases, when $\delta k' < 0$, only one mode remains mid-gap; another becomes extremely close to the lower bulk band, resulting in slow spatial decay from the domain boundary; and the third completely disappears, as shown in Figure 7i. Meanwhile, when $\delta k' > 0$, the two surviving in-gap states are located at the mid-gap state, with rapid spatial decay (Figure 7j), and the third in-gap mode no longer exists within the bulk bandgap. Instead, it migrates to above the top bulk band. The SFT in Figure 7k further proves that only the in-gap mode adjacent to the bulk when $\delta k' = -0.9$ is narrower than the other SFT peaks, suggesting more leakage into the bulk than in the other case, which is evident in Figure 7i.

3. Conclusions

In this work, we used Su–Schrieffer–Heeger models to thoroughly compare the effect of various boundary conditions on the survivability of in-gap states within bulk bandgaps and their relationship with topologically protected edge/domain-wall states. We found that the in-gap edge states never exist when lattice boundaries are free since the stiffness matrix largely deviates from being chiral. The occasional observed localized edge modes only occur by accident due to specific spring arrangements. They are not topologically protected and leak extensively into the bulk and are therefore vulnerable to disturbances such as manufacturing flaws and impurities, making them difficult to implement in applications. On the other hand, fixing the free ends to the ground with proper spring constants to ensure the chirality of the stiffness matrix guarantees the topologically protected edge states when the lattice arrangement is topological. The edge states are also strongly localized on the edges. Meanwhile, the in-gap domain-wall states formed by two topologically different

domains are much more tolerant to the non-chirality of the stiffness matrix, although not all in-gap states will survive with a large difference in the third-nearest neighbors. Interestingly, when the domain-wall mass is connected by stiffer springs, the mid-gap states are always retained and preserve most of the topological features, such as rapid spatial decay, which is not the case when the domain-wall mass is connected by softer springs. These topological-like in-gap states, although no longer topological in strict terms, are mostly robust against large perturbations and are henceforth more applicable in engineering designs where the localization of vibration within a narrow spectrum is desired, such as drug delivery [49,50] and quantum information processing using phonons [51].

Although we used discrete mass-spring models in our study, the conclusions may offer insights into the truncation effect on vibration in continuum periodic systems [30,52] or functionally graded materials [53] for more practical engineering applications.

Author Contributions: Conceptualization, J.M.; methodology, A.R.A. and J.M.; software, A.R.A. and J.M.; validation, J.M.; formal analysis, J.M.; investigation, A.R.A. and J.M.; resources, A.R.A. and J.M.; data curation, J.M.; writing—original draft, A.R.A. and J.M.; Writing—review and editing, J.M.; visualization, J.M.; supervision, J.M.; project administration, J.M. All authors have read and agreed to the published version of the manuscript.

Funding: This research received no external funding.

Data Availability Statement: Data are contained within the article.

Conflicts of Interest: The authors declare no conflicts of interest.

Abbreviations

The following abbreviations are used in this manuscript:

TI	Topological insulator
1D	One-dimension(al)
SSH	Su–Schrieffer–Heeger
TPES	Topologically protected edge state
TPDWS	Topologically protected domain-wall state
BNN	Beyond-nearest neighbor
TNN	Third-nearest neighbor
SIS	Space-inversion symmetry
IBZ	Irreducible Brillouin zone

References

- Hasan, M.Z.; Kane, C.L. Colloquium: Topological insulators. *Rev. Mod. Phys.* **2010**, *82*, 3045. [[CrossRef](#)]
- He, M.; Sun, H.; He, Q.L. Topological insulator: Spintronics and quantum computations. *Front. Phys.* **2019**, *14*, 43401. [[CrossRef](#)]
- Lu, L.; Joannopoulos, J.D.; Soljačić, M. Topological photonics. *Nat. Photonics* **2014**, *8*, 821–829. [[CrossRef](#)]
- Yang, Y.; Xu, Y.F.; Xu, T.; Wang, H.X.; Jiang, J.H.; Hu, X.; Hang, Z.H. Visualization of a unidirectional electromagnetic waveguide using topological photonic crystals made of dielectric materials. *Phys. Rev. Lett.* **2018**, *120*, 217401. [[CrossRef](#)]
- Wang, H.; Gupta, S.K.; Xie, B.; Lu, M. Topological photonic crystals: A review. *Front. Optoelectron.* **2020**, *13*, 50–72. [[CrossRef](#)] [[PubMed](#)]
- Tang, G.J.; He, X.T.; Shi, F.L.; Liu, J.W.; Chen, X.D.; Dong, J.W. Topological photonic crystals: Physics, designs, and applications. *Laser Photonics Rev.* **2022**, *16*, 2100300. [[CrossRef](#)]
- Hafezi, M.; Mittal, S.; Fan, J.; Migdall, A.; Taylor, J. Imaging topological edge states in silicon photonics. *Nat. Photonics* **2013**, *7*, 1001–1005. [[CrossRef](#)]
- Zhang, R.X.; Liu, C.X. Topological magnetic crystalline insulators and corepresentation theory. *Phys. Rev. B* **2015**, *91*, 115317. [[CrossRef](#)]
- Tokura, Y.; Yasuda, K.; Tsukazaki, A. Magnetic topological insulators. *Nat. Rev. Phys.* **2019**, *1*, 126–143. [[CrossRef](#)]
- Malki, M.; Uhrig, G. Topological magnetic excitations. *Europhys. Lett.* **2020**, *132*, 20003. [[CrossRef](#)]
- Wang, P.; Lu, L.; Bertoldi, K. Topological phononic crystals with one-way elastic edge waves. *Phys. Rev. Lett.* **2015**, *115*, 104302. [[CrossRef](#)] [[PubMed](#)]
- Tian, Z.; Shen, C.; Li, J.; Reit, E.; Bachman, H.; Socolar, J.E.; Cumber, S.A.; Jun Huang, T. Dispersion tuning and route reconfiguration of acoustic waves in valley topological phononic crystals. *Nat. Commun.* **2020**, *11*, 762. [[CrossRef](#)]

13. Ma, J. Phonon Engineering of Micro-and Nanophononic Crystals and Acoustic Metamaterials: A Review. *Small Sci.* **2023**, *3*, 2200052. [[CrossRef](#)]
14. Ma, J.; Zhou, D.; Sun, K.; Mao, X.; Gonella, S. Edge modes and asymmetric wave transport in topological lattices: Experimental characterization at finite frequencies. *Phys. Rev. Lett.* **2018**, *121*, 094301. [[CrossRef](#)] [[PubMed](#)]
15. Ma, J.; Sun, K.; Gonella, S. Valley hall in-plane edge states as building blocks for elastodynamic logic circuits. *Phys. Rev. Appl.* **2019**, *12*, 044015. [[CrossRef](#)]
16. Zhou, D.; Ma, J.; Sun, K.; Gonella, S.; Mao, X. Switchable phonon diodes using nonlinear topological Maxwell lattices. *Phys. Rev. B* **2020**, *101*, 104106. [[CrossRef](#)]
17. Rajabpoor Alisepahi, A.; Sarkar, S.; Sun, K.; Ma, J. Breakdown of conventional winding number calculation in one-dimensional lattices with interactions beyond nearest neighbors. *Commun. Phys.* **2023**, *6*, 334. [[CrossRef](#)]
18. Kane, C.L.; Lubensky, T.C. Topological boundary modes in isostatic lattices. *Nat. Phys.* **2014**, *10*, 39–45. [[CrossRef](#)]
19. Paulose, J.; Chen, B.G.G.; Vitelli, V. Topological modes bound to dislocations in mechanical metamaterials. *Nat. Phys.* **2015**, *11*, 153–156. [[CrossRef](#)]
20. Rocklin, D.Z.; Zhou, S.; Sun, K.; Mao, X. Transformable topological mechanical metamaterials. *Nat. Commun.* **2017**, *8*, 14201. [[CrossRef](#)]
21. Rocklin, D.Z.; Chen, B.G.G.; Falk, M.; Vitelli, V.; Lubensky, T. Mechanical Weyl modes in topological Maxwell lattices. *Phys. Rev. Lett.* **2016**, *116*, 135503. [[CrossRef](#)] [[PubMed](#)]
22. Bilal, O.R.; Süssstrunk, R.; Daraio, C.; Huber, S.D. Intrinsically polar elastic metamaterials. *Adv. Mater.* **2017**, *29*, 1700540. [[CrossRef](#)] [[PubMed](#)]
23. Süssstrunk, R.; Huber, S.D. Observation of phononic helical edge states in a mechanical topological insulator. *Science* **2015**, *349*, 47–50. [[CrossRef](#)] [[PubMed](#)]
24. Nash, L.M.; Kleckner, D.; Read, A.; Vitelli, V.; Turner, A.M.; Irvine, W.T. Topological mechanics of gyroscopic metamaterials. *Proc. Natl. Acad. Sci. USA* **2015**, *112*, 14495–14500. [[CrossRef](#)]
25. Mousavi, S.H.; Khanikaev, A.B.; Wang, Z. Topologically protected elastic waves in phononic metamaterials. *Nat. Commun.* **2015**, *6*, 8682. [[CrossRef](#)]
26. Pal, R.K.; Ruzzene, M. Edge waves in plates with resonators: An elastic analogue of the quantum valley Hall effect. *New J. Phys.* **2017**, *19*, 025001. [[CrossRef](#)]
27. Al Ba'ba'a, H.; Nouh, M.; Singh, T. Formation of local resonance band gaps in finite acoustic metamaterials: A closed-form transfer function model. *J. Sound Vib.* **2017**, *410*, 429–446. [[CrossRef](#)]
28. Bastawrous, M.V.; Hussein, M.I. Closed-form existence conditions for bandgap resonances in a finite periodic chain under general boundary conditions. *J. Acoust. Soc. Am.* **2022**, *151*, 286–298. [[CrossRef](#)]
29. Allein, F.; Anastasiadis, A.; Chaunsali, R.; Frankel, I.; Boechler, N.; Diakonov, F.K.; Theocharis, G. Strain topological metamaterials and revealing hidden topology in higher-order coordinates. *Nat. Commun.* **2023**, *14*, 6633. [[CrossRef](#)]
30. Rosa, M.I.; Davis, B.L.; Liu, L.; Ruzzene, M.; Hussein, M.I. Material vs. structure: Topological origins of band-gap truncation resonances in periodic structures. *Phys. Rev. Mater.* **2023**, *7*, 124201. [[CrossRef](#)]
31. Kuo, J.Y.; Lee, T.Y.; Chiu, Y.C.; Liao, S.R.; Kao, H.C. SSH coupled-spring systems. *arXiv* **2023**, arXiv:2310.00547.
32. Coutant, A.; Sivadon, A.; Zheng, L.; Achilleos, V.; Richoux, O.; Theocharis, G.; Pagneux, V. Acoustic Su-Schrieffer-Heeger lattice: Direct mapping of acoustic waveguides to the Su-Schrieffer-Heeger model. *Phys. Rev. B* **2021**, *103*, 224309. [[CrossRef](#)]
33. Li, X.; Meng, Y.; Wu, X.; Yan, S.; Huang, Y.; Wang, S.; Wen, W. Su-Schrieffer-Heeger model inspired acoustic interface states and edge states. *Appl. Phys. Lett.* **2018**, *113*, 203501. [[CrossRef](#)]
34. Joubaneh, E.F.; Ma, J. Symmetry effect on the dynamic behaviors of sandwich beams with periodic face sheets. *Compos. Struct.* **2022**, *289*, 115406. [[CrossRef](#)]
35. Yang, S.; Chang, H.; Wang, Y.; Yang, M.; Sun, T. A phononic crystal suspension for vibration isolation of acoustic loads in underwater gliders. *Appl. Acoust.* **2024**, *216*, 109731. [[CrossRef](#)]
36. Bendsoe, M.P.; Sigmund, O. *Topology Optimization: Theory, Methods, and Applications*; Springer Science & Business Media: Berlin/Heidelberg, Germany, 2003.
37. Hussein, M.I.; Hamza, K.; Hulbert, G.M.; Saitou, K. Optimal synthesis of 2D phononic crystals for broadband frequency isolation. *Waves Random Complex Media* **2007**, *17*, 491–510. [[CrossRef](#)]
38. Chen, Y.; Kadic, M.; Wegener, M. Roton-like acoustical dispersion relations in 3D metamaterials. *Nat. Commun.* **2021**, *12*, 3278. [[CrossRef](#)]
39. Iglesias Martínez, J.A.; Groß, M.F.; Chen, Y.; Frenzel, T.; Laude, V.; Kadic, M.; Wegener, M. Experimental observation of roton-like dispersion relations in metamaterials. *Sci. Adv.* **2021**, *7*, eabm2189. [[CrossRef](#)]
40. Iorio, L.; De Ponti, J.M.; Maspero, F.; Ardito, R. Roton-like dispersion via polarisation change for elastic wave energy control in graded delay-lines. *J. Sound Vib.* **2024**, *572*, 118167. [[CrossRef](#)]
41. Cui, J.G.; Yang, T.; Niu, M.Q.; Chen, L.Q. Tunable roton-like dispersion relation with parametric excitations. *J. Appl. Mech.* **2022**, *89*, 111005. [[CrossRef](#)]
42. Wang, K.; Chen, Y.; Kadic, M.; Wang, C.; Wegener, M. Nonlocal interaction engineering of 2D roton-like dispersion relations in acoustic and mechanical metamaterials. *Commun. Mater.* **2022**, *3*, 35. [[CrossRef](#)]

43. Zhu, Z.; Gao, Z.; Liu, G.G.; Ge, Y.; Wang, Y.; Xi, X.; Yan, B.; Chen, F.; Shum, P.P.; Sun, H.X.; et al. Observation of multiple rotons and multidirectional roton-like dispersion relations in acoustic metamaterials. *New J. Phys.* **2022**, *24*, 123019. [[CrossRef](#)]
44. Grundmann, M. Topological States Due to Third-Neighbor Coupling in Diatomic Linear Elastic Chains. *Phys. Status Solidi B* **2020**, *257*, 2000176. [[CrossRef](#)]
45. Chen, H.; Nassar, H.; Huang, G. A study of topological effects in 1D and 2D mechanical lattices. *J. Mech. Phys. Solids* **2018**, *117*, 22–36. [[CrossRef](#)]
46. Liu, H.; Huang, X.; Yan, M.; Lu, J.; Deng, W.; Liu, Z. Acoustic Topological Metamaterials of Large Winding Number. *Phys. Rev. Appl.* **2023**, *19*, 054028. [[CrossRef](#)]
47. Zak, J. Berry's phase for energy bands in solids. *Phys. Rev. Lett.* **1989**, *62*, 2747. [[CrossRef](#)] [[PubMed](#)]
48. Jackiw, R.; Rebbi, C. Solitons with fermion number 1/2. *Phys. Rev. D* **1976**, *13*, 3398. [[CrossRef](#)]
49. Vanden-Hehir, S.; Tipping, W.J.; Lee, M.; Brunton, V.G.; Williams, A.; Hulme, A.N. Raman imaging of nanocarriers for drug delivery. *Nanomaterials* **2019**, *9*, 341. [[CrossRef](#)]
50. Yeo, L.Y.; Friend, J.R.; McIntosh, M.P.; Meeusen, E.N.; Morton, D.A. Ultrasonic nebulization platforms for pulmonary drug delivery. *Expert Opin. Drug Deliv.* **2010**, *7*, 663–679. [[CrossRef](#)]
51. Bienfait, A.; Satzinger, K.J.; Zhong, Y.; Chang, H.S.; Chou, M.H.; Conner, C.R.; Dumur, É.; Grebel, J.; Peairs, G.A.; Povey, R.G.; et al. Phonon-mediated quantum state transfer and remote qubit entanglement. *Science* **2019**, *364*, 368–371. [[CrossRef](#)]
52. Al Ba'ba'a, H.B.; Willey, C.L.; Chen, V.W.; Juhl, A.T.; Nouh, M. Theory of Truncation Resonances in Continuum Rod-Based Phononic Crystals with Generally Asymmetric Unit Cells. *Adv. Theory Simul.* **2023**, *6*, 2200700. [[CrossRef](#)]
53. Kuznetsov, S.V. Guided waves in FG plates: Appearing phase velocity gaps. *Z. Angew. Math. Und Phys.* **2022**, *73*, 127. [[CrossRef](#)]

Disclaimer/Publisher's Note: The statements, opinions and data contained in all publications are solely those of the individual author(s) and contributor(s) and not of MDPI and/or the editor(s). MDPI and/or the editor(s) disclaim responsibility for any injury to people or property resulting from any ideas, methods, instructions or products referred to in the content.